

NGC 4244: A LOW MASS GALAXY WITH A FALLING ROTATION CURVE AND A FLARING GAS LAYER

Rob P. Olling

Columbia University, New York,

now at Dept. of Physics, University of Southampton, Southampton S17 1BJ, U.K.

olling@astro.soton.ac.uk

To be published in the Aug. 1996 issue of the *Astronomical Journal*

ABSTRACT

I present sensitive high resolution VLA B, C, and D array observations of the almost edge-on Scd galaxy NGC 4244 in the 21-cm spectral line of neutral atomic hydrogen. The gas layer of NGC 4244 is rather symmetric in all respects, i.e. the surface density distribution, flaring and warping. This symmetry allows for a reliable determination of the rotation curve, despite the fact that the galaxy is close to edge-on. The rotation curve rises slowly in the inner 6 kpc, is roughly constant at 100 km s^{-1} out to 10 kpc, and decreases in Keplerian fashion by 15% at the last measured point at 14 kpc. The rotation curve constrains the stellar mass-to-light ratio to lie between 50 and 100% of the “maximum-disk” value.

A new technique is presented to determine simultaneously the inclination and the thickness of the gas layer from high resolution H I observations. This procedure uses the apparent widths at many azimuths (many channels) and can be used at inclinations as low as 60° . Kinematic information is used to separate flaring from warping. The inclination of the unwarped disk is about 84.5° , while the small warp coincides with a decreasing inclination (to $82.5 \pm 1^\circ$). The data indicates that at large radii the disk warps back to the plane defined by the inner disk. The measured gaseous velocity dispersion is roughly constant within the optical disk ($8.5 \pm 1 \text{ km s}^{-1}$) and increases slightly beyond.

On both sides of the galaxy the thickness of the gas layer increases gradually from $\sim 400 \text{ pc}$ at 5 kpc to $\sim 1.5 \text{ kpc}$ at the last measured point (at 13 kpc). The strong gradients in the *inferred* thickness which bracket the spiral arms probably result from streaming motions associated with the arms and are not intrinsic to the galaxy. In an accompanying paper (AJ, Aug. 1996) I use the measurements presented in this paper to infer that the dark matter halo of NGC 4244 is highly flattened.

1. INTRODUCTION

In a previous paper, Paper I (Olling 1995), it was shown that measurements of the radial variation of the thickness of gas layers (flaring) can be used to constrain the shape of the dark matter (DM) halo. This is accomplished by comparing the measured flaring with that expected from a self-gravitating gaseous disk in a potential generated by the stellar disk and (flattened) DM halo. Here, high resolution H I observation of the nearby, almost edge-on, Scd galaxy NGC 4244 are presented. Using these observations I determine the rotation curve, the flaring, the velocity dispersion, and the radial surface density distribution of the gas. In the accompanying paper (Paper III, AJ, 1996, ..., ...) I will apply the method presented in Paper I to determine the flattening of the dark matter halo of NGC 4244 using the essential parameters as derived in this paper.

In a study similar to the present one, Rupen (1991a) analyzed high resolution H I observations of two edge-on galaxies, NGC 4565 and NGC 891. Due to the increased sensitivity of the VLA, sensitive high resolution H I observations, as pioneered by Rupen (1991b), can now be routinely obtained and processed. The high resolution H I data presented in this paper are sensitive enough to determine the gaseous velocity dispersion and probe the region beyond the optical disk where the thickness of the gas layer is most sensitive to the shape of the DM halo. The new technique to determine the thickness of the gas layer (presented in Sec. 5.) complements an existing procedure specific to the case of strong spiral structure in the H I (Braun 1991), and is more general than the method employed by Irwin & Seaquist (1991).

NGC 4244 is an intermediate mass system with a rotation speed of about 100 km/s. Its proximity (3.6 Mpc) results in the high linear spatial resolution (17.5 pc/arcsec) which is necessary to successfully determine both the verti-

cal structure of the gaseous disk and the rotation curve in the inner parts of the galaxy. The large inclination of NGC 4244 with respect to the line of sight, about 84.5 degrees, in combination with the symmetric surface density distribution, allows for an accurate determination of the rotation curve. NGC 4244 is one of the few galaxies to show, on both sides, the characteristic drop in rotation velocity beyond the optical disk.

The outline of this paper is as follows: in Sec. 2. I summarize current observational knowledge of NGC 4244. The H I observations are presented in Sec. 3. and the parameters derived therefrom in Sec. 4.. A new technique to derive the thickness and inclination of the gas layer is outlined in Sec. 5.1., and is applied in Sec. 5.2.. The results are discussed in Sec. 6..

2. THE GALAXY NGC 4244

NGC 4244 is a small almost edge-on ScdIII galaxy in which individual stars and H II regions can be resolved (Sandage & Bedke 1994). Surface brightness photometry (van der Kruit & Searle 1981a) reveals that the radial light distribution is close to exponential till about five optical scale lengths, where it cuts off sharply (see also Fig. 2). The vertical scale height of the light is constant with radius, while no thick disk is present. The very faint bulge ($\mu_K(r_e) = 23.05 \text{ mag/arcsec}^2$) with an effective radius of $140''$ (Bergstrom *et al.* 1992) is dynamically insignificant.

There are several indications that the current star formation rate is very low in NGC 4244. Only very low radio continuum emission (Condon 1987) and little H α emission (Walterbos 1994, private communications) have been detected, while upper limits have been set on X-ray emission (Bregman & Glassgold 1982) and emission from highly ionized halo gas (Deharveng *et al.* 1986). Very faint radio continuum emission extends along the plane of the galaxy from $2'5$ north-east (NE) to $2'$ south-west (SW)

of the center. The $60\mu\text{m}$ emission is enhanced in this region as well (Rice 1993). In contrast to most galaxies (Bica & Helou 1990), NGC 4244's 20 cm radio continuum emission is not more extended than the $60\mu\text{m}$ emission. The weak CO emission (Sage 1993), coincident with the radio continuum emission, amounts to $2.2 \times 10^7 M_\odot$ of H_2 (50% of the H I mass in this region). The H_2 radial surface density distribution is calculated with the Abel inversion technique (Sec. 4.1.) and is consistent with a Gaussian ring centered at 1.3 kpc, with a FWHM of 1.6 kpc and an amplitude of $1.6 M_\odot\text{pc}^{-2}$.

Throughout this paper the distance to NGC 4244 is taken to be 3.6 Mpc, consistent with the IR-Tully-Fisher distance (3.7 Mpc, Aaronson *et al.* 1986) and the "hydrogen counterpart" of the Tully-Fisher distance (3.6 Mpc) as defined by Broeils (1992, Chapter 3). NGC 4244 is the second brightest member of a group of dwarf galaxies: the CVn I (de Vaucouleurs 1975) or B4 (Kraan-Korteweg & Tammann 1979) group with 21 catalogued members. This group has a radius of 1 Mpc, an average density of 4.5 Mpc^{-3} , and a total luminosity of $8.9 \times 10^9 L_{\odot,B}$. The nearest catalogued neighbor is the SmIV galaxy NGC 4190 at a projected distance of 81 kpc. This group is rather elongated (axial ratio ~ 3), with the position angle of the long axis at -18° , 66° from the plane of NGC 4244. The observation presented in this paper (Sec. 3.1.) fail to detect gas rich companions more massive than $10^7 M_\odot$ within 45 kpc.

Figure 1 shows the optical (grey scale) image from IIIaJ photographic observations (van der Kruit & Searle 1981a) and a total hydrogen map. The orientation of the weak dustlane suggests that the eastern side of the galaxy is the far side and thus least affected by absorption. The intrinsic radial surface brightness distribution, $L(R)$, is derived by applying the Abel-inversion technique (Sec. 4.1.) to four different strips parallel to the major axis, after removal of foreground stars. The first strip contains all light perpen-

dicular to the minor axis (top profile in Fig. 2). The second strip contains all light within 420 pc (twice the vertical exponential scale height, z_e) from the midplane. The third and fourth strips are determined from those parts which are further than 420 pc from the midplane (east and west respectively). As the region which is affected by dust extinction lies generally close to the plane ($z \lesssim 1/2 z_e$; Peletier *et al.* 1995), the third and fourth strips are expected to be free of extinction effects. All four profiles indicate a radially exponential light distribution with the same radial scale length (h_R) of 2.0 kpc, slightly larger than the value derived by van der Kruit & Searle (1981a)¹. Thus, the overall light distribution is probably not much affected by extinction (the adopted fit is indicated by the filled circles). As noticed by van der Kruit & Searle (1981a), the stellar disk is truncated at somewhat different radial distances on the two sides of the galaxy. The IIIaJ-magnitudes are converted to B-magnitudes assuming a $(B-V)=0.7$ as appropriate for the old disk (Bottema 1989). Some parameters of this galaxy are listed in Table 1.

3. H I OBSERVATIONS

NGC 4244 was observed with the VLA² (Napier *et al.* 1983), in the 10 km (B), 3 km (C), and 1 km (D) arrays for a total of about 14 hours. The data from 1989 and 1990 were taken as part of a project aimed at doing a multi-wavelength high resolution study of the interstellar medium in nearby galaxies (Braun 1995). The observing parameters are summarized in Table 2.

Standard calibration procedures were followed. After removal of some data affected by inter-

¹All the linear distances derived by van der Kruit & Searle (1981a), who use a distance of 5 Mpc (Sandage & Tammann, 1975), are scaled to the adopted distance for NGC 4244, 3.6 Mpc.

²The VLA of the National Radio Astronomy Observatory is a facility of the National Science Foundation operated under cooperative agreement by Associated Universities, Inc.

ference³ the data were combined in the UV plane. The primary flux calibrator was 3C 286, with an assumed flux at 1418 MHz of 14.86 Jy. A heavily tapered continuum image was made using 5 line-free channels on both sides of the band. The rms noise in this image is 0.94 mJy beam⁻¹ at a resolution of 80'' x 77''. Several background sources but no extended radio continuum emission was detected from NGC 4244 itself down to a 3 sigma limit of 2.8 mJy beam⁻¹, consistent with a peak flux of 1.4 mJy as determined by Condon (1987) and Hummel *et al.*'s (1984) non-detection at 610 MHz. A strong background source about 7' NE of NGC 4244 is probably the reason for the much stronger detection reported by Schlickeiser *et al.* (1984).

For the two high resolution data sets the sensitivities listed in Table 2 correspond to roughly $3 \times 10^4 M_{\odot}$ beam⁻¹ channel⁻¹ at the field center, while the two low-resolution sets are about three times more sensitive as a result of the interim upgrade of the VLA receivers. To bring out emission at different scales, images of the line emission were made with different tapering.

3.1. Results

Assuming low optical depth the total amount of neutral hydrogen is arrived at by adding the flux containing areas in the channel maps. The validity of this assumption is checked in Appendix D.. The flux containing areas are defined to be those regions which have a flux larger than $\sim 1.2\sigma$ in a smoothed version of the spectral line cube (smoothed to a four and three times lower resolution, spatially and in velocity respectively). The high and low-resolution total H I distributions are presented in Fig. 3. The images have been rotated 48° clockwise, so that the upper part is the north-eastern side. Both the high and low resolution data show a warp starting at the edge of the optical disk (about 9

arcmin from the center). The H I distribution of NGC 4244 is rather symmetric apart from the “popped blister” located just below the major axis about four arcmin to the north-east. A recent star formation event might be responsible for this feature as it coincides with peaks in the radio continuum and IRAS emission.

The low resolution, primary beam corrected, total intensity image yields a total H I mass of $(1.29 \pm 0.05) \times 10^9 M_{\odot}$. The north-eastern part contains 51% of the total H I mass, the south-western part amounts to 49%. The hydrogen mass determined from the global profile (the flux as a function of velocity, Fig. 4), $(1.4 \pm 0.1) \times 10^9 M_{\odot}$, is consistent with the determination from the total H I map. The H I mass listed in Table 3 is the average of the total H I and global profile values, where the error equals half the difference.

From the global profile a systemic velocity (the mean of the 10%, 20% and 50% points) of 244.4 ± 0.3 km s⁻¹ is determined, in agreement with the value determined by Huchtmeier & Seiradakis (1985). As a result of the asymmetry in the H I distribution, the receding part has a higher peak value than the approaching part. The position at the major axis where the recession velocity equals the systemic velocity is offset by $7''.4 \pm 0''.6$ towards the south-west, which agrees well with the central position of the H I as determined in Sec. 4.1..

Within 45 kpc from the pointing center, no companions were detected down to a five sigma level of $10^5 M_{\odot}$ channel⁻¹ at the center (or $1.6 \times 10^7 M_{\odot}$ channel⁻¹ at 45 kpc).

Fig. 5 shows a composite of the high resolution (28''x10'' or 490x177 pc along the major and minor axes respectively) and intermediate resolution (38''x38'') channel maps. The maps are combined such that the channels with the same speed relative to the systemic velocity are present in one frame (after having blanked those areas without emission). The receding part of NGC 4244 is the south-western part (negative X-values), the north-eastern part is approaching.

³In particular the 1992 D-array daytime observations required extensive UV-editing due to solar interference.

The low velocity channels, which would overlap if presented in this manner, are presented individually. One local irregularity is clearly visible: the $+4'$ “hole” found in the total H I map can be seen in the frames labeled 17, 18, and 19.

Each map shows a characteristic “filled V” shape. Two different mechanisms can cause such shapes. First of all it reflects the flaring of the gaseous disk. The other contributing factor is kinematic in nature: the “butterfly” pattern (seen in channel maps of less inclined systems, e.g., Bosma 1981) seen almost edge-on. In Sec. 5.1. I present a new technique to disentangle these two effects. Classically the flaring is measured in the edge channels, i.e. at velocities of $(V_{\text{sys}} \pm V_{\text{rot,max}})$ (Sancisi & Allen 1979; van der Kruit 1981; Rupen 1991a). Because NGC 4244 is not exactly edge-on and because the velocity edge depends on radius (due to the falling rotation curve), the apparent widths can not be easily interpreted in terms of an intrinsic vertical scale height. Furthermore, systematic errors, e.g. due to non-circular motions are largest in the edge channels (Appendix C.). The channels ± 18 are the edge channels between about $5'$ and $9'$. For this radial range, the receding side exhibits a more-or-less regular increase of apparent width, but on the approaching side this effect is not evident. This difference can easily arise from local effects such as arm inter-arm surface density differences, holes, bubbles, and streaming motions. The new thickness-and-inclination determination technique outlined in Sec. 5.1. minimizes the effects of such irregularities.

A rather regular warp, starting just before the optical edge of the galaxy, is seen in the channel maps. The channels $\pm 16, \pm 17$, and ± 18 show the strongest warping at large radii. The position angle of the warp is determined by tracing the major axis of emission as a function of major axis distance. Within the optical disk, the position angle of the centroid is constant at 48° east of north. At a radius of $8'$, the position angle begins to change linearly to reach 43° at $13'$.

Because no clear butterfly pattern is seen in the warped region, the warp is likely to be the result of a change in position angle rather than in inclination. This is confirmed by the derived radial variation of the inclination (Fig. 13).

4. INFERRED PROPERTIES

In this section several properties of the gas⁴ layer will be determined: the radial surface density distribution ($\Sigma_{\text{gas}}(R)$), the rotation curve ($V_{\text{rot}}(R)$), and the radial variation of the gaseous velocity dispersion ($\sigma_{\text{gas}}(R)$). All these quantities are required to make self-consistent predictions of the radial variation of the thickness of the gas layer (Paper I, Paper III). Furthermore, with the aim to gauge the reliability of the determination of these properties, these quantities are used to compare the VLA observations with simulated observations of NGC 4244 (Appendix B.).

Integrating the total hydrogen along the minor axis results in a major axis H I profile ($\Lambda(x)$). The inner $4'$ of this profile are symmetric about a point located $6''.9 \pm 0''.6$ to the south-west (along the major axis) of the catalogued position. Similarly, the location of the midplane is offset by $2''.2 \pm 0''.5$ to the south-east. In the rest of this paper I assume that NGC 4244’s center is located at the centroid of the H I -distribution: $\alpha = 12^{\text{h}} 15^{\text{m}} 9^{\text{s}}.7$, $\delta = 38^\circ 4' 59''.4$, which position is listed in Table 3. This position agrees with the kinematic center determined in Sec. 3.1..

4.1. The H I Surface Density Distribution

I describe the line of sight deconvolution necessary to determine the radial surface density distribution after introducing the coordinate systems used. First there is the coordinate system centered on the center of the galaxy: (x, y, z) in

⁴Unless otherwise noted, the term “gas” refers to H I in an observational context, and to the sum of H I, H₂ and He in a dynamical context.

Cartesian coordinates and (R, θ, z) in polar coordinates (with $\theta = 0$ being the intersection of the plane of the sky with the plane of the galaxy, and with z the vertical coordinate). In the observers coordinate frame, x and d are coincident with the major and minor axes of the inner, unwarped, part of the disk. The projection of the line of sight onto the (unwarped part of the) plane of the galaxy is parallel to the y -axis.

I determine an approximation to the H I profile (the total H I distribution summed perpendicular to the major axis) by summing the emission over the d -axis. Because of the warp the x -coordinate does not truly trace the major axis (x'). However, since $x' = \sqrt{x^2 + d^2}$ does not differ significantly for the small warp of NGC 4244 ($d \leq 1$ kpc for $x \leq 13$ kpc), the derived density distribution is not affected. The integration⁵ of the volume density along the line of sight and perpendicular to the major axis, which yields the H I profile, can be written as an integration of the true surface density along the y -axis:

$$\begin{aligned} \Lambda(x') &\approx \int_{-\infty}^{+\infty} dy \Sigma_{\text{gas}} \left(\sqrt{x^2 + y^2} \right) \\ &= 2 \times \int_x^{\infty} \frac{R \Sigma_{\text{gas}}(R)}{\sqrt{R^2 - x^2}} dR \quad (\text{M}_{\odot}/\text{pc}). \quad (1) \end{aligned}$$

Inversion of this Abel integral [e.g., Binney & Tremaine, Eq. (1B-59b)] yields the radial surface density distribution

$$\begin{aligned} \Sigma_{\text{gas}}(R) &= -\frac{1}{\pi} \times \\ &\int_R^{\infty} \frac{1}{\sqrt{(x^2 - R^2)}} \frac{d\Lambda(x)}{dx} dx \quad (\text{M}_{\odot}/\text{pc}^2). \quad (2) \end{aligned}$$

This procedure can be applied at any wavelength for any inclination provided that the optical depth is low, the galaxy is not warped and if it is axisymmetric. Note that similar techniques were used to determine the surface brightness distribution of Virgo spirals from ‘‘pencil-beam’’ H I data (Warmels 1988) and the mass-to-light ratio of elliptical galaxies (i.e., Schwarzschild 1954; Binney

& Mamon 1982). Adding realistic noise to a simulated spectral line cube (Appendix B.) and applying Eq. (2) yields the input $\Sigma_{\text{gas}}(R)$. Thus, the derivation of the surface density distribution is not sensitive to noise. However, if the signal to noise ratio is poor, it may be preferable to use the iterative technique proposed by Warmels (1988).

$\Sigma_{\text{gas}}(R)$ is derived from a combination of the high and low resolution $\Lambda(x)$ curves and is presented in Fig. 6. Negative surface densities at small radii occur unless the two sides of the $\Lambda(x)$ profile are averaged over the inner ~ 1.5 kpc. Thus this method does not recover the true $\Sigma_{\text{gas}}(R, \theta)$ but it can find an azimuthally symmetric density distribution consistent with the observations: it serves as a reasonable approximation to the true distribution. Integrating the $\Sigma(R)$ profiles out to 15.8 kpc (where the surface density equals $0.02 \text{ M}_{\odot}\text{pc}^{-2}$), I find $1.4 \times 10^9 \text{ M}_{\odot}$: the Abel inversion technique conserves flux.

Several strong (up to a factor 3) density enhancements (~ 1 kpc wide), possibly spiral arms, are present. In the inner 4 kpc the south-western and north-eastern density distributions are very similar. Beyond 10 kpc the surface density decreases in an exponential manner with a scale length of roughly 1.36 kpc. No sharp cutoff in the H I column density is seen *above* the 3σ detection limit ($5 \times 10^{18} \text{ cm}^{-2}$). We see that the surface density distribution is rather symmetric (see also Sec. 5.2.), except in the 6 - 8 kpc region. It might be that this surface density difference causes differences in the observed flaring (Fig. 13) as a result of the different self-gravity at these points.

4.2. The Rotation Curve and the Velocity Dispersion of the Gas

Figure 7 shows the intensity as a function of velocity and position along the major axis (summed over the minor axis). The rotation curve and velocity dispersion of NGC 4244 are derived from this plot. The maximum relative velocity outline corresponds roughly to the rotation

⁵Assuming low optical depth, see Appendix D..

speed minus twice the velocity dispersion in the tangential direction. Approximations to the rotation speed and velocity dispersion were determined by fitting a single Gaussian to the extreme velocity envelope. These approximations have been corrected for instrumental, line-of-sight integration, and beam smearing effects, as detailed in Appendix A..

Figure 8 shows NGC 4244’s smearing corrected intrinsic tangential dispersion as derived from the high, intermediate and low resolution data sets, which sample different ranges in galactocentric radius. For each set of measurements, both sides yield dispersions generally equal to within the errors. The errors on the values extracted from the $10''$ data set are large because the signal to noise ratio is relatively low. The average dispersion curve is the weighted average of the measurements obtained at the two sides ($38''$ data set for $R \in (9, 13]$ kpc, and $55''$ beyond). For radii smaller than 9 kpc I also average the measurements from the Hanning-smoothed $10''$ and $38''$ data sets since these data arise from essentially independent measurements (B & D array, respectively).

In Fig. 9 I present the line-of-sight and beam-smearing corrected rotation curves for both sides of the galaxy. Apart from the region between 2.5 and 7.5 kpc, the rotation curves are equal to within the errors. The drop in the north-eastern rotation curve seen between 2.5 and 5.5 kpc is clearly a result of a local phenomenon (described above): there the adopted rotation curve follows the south-western curve ($10'' \times 10''$) till 4.5 kpc. The adopted rotation curve between 4.5 and 6 kpc is a smooth junction of the adjacent regions: here the rotation speeds as determined from the XV plots are probably influenced by the strong H I peak at 5.5 kpc (see Appendix A. for a discussion). The 6 to 7.5 kpc region, on the south-western side, corresponds to the region where the B-band surface brightness is depressed by a factor of about 10. Therefore, I choose the intrinsic rotation curve to follow the north-eastern curve

in this range of galactocentric radii ($38'' \times 38''$). Taking these modifications into account leads to the adopted intrinsic rotation curve (indicated by the filled circles in Figure 9), which is minimally affected by non-circular motions.

Because of the large inclination, small changes thereof are not important for the derivation of the rotation curve. The maximum amplitude of the rotation velocity is about 100 km s^{-1} and starts dropping significantly beyond R_{max} , the edge of the optical disk. At a distance of 14 kpc the rotation speed has dropped to 85 km s^{-1} . Huchtmeier (1975) finds, using a $9'$ beam, that the H I extends out to $18'$ and determines a rotation speed of $85 \pm 5 \text{ km s}^{-1}$ at that distance. The measurements presented in this paper do not confirm this detection. The symmetry between the two sides indicates that the gas is likely to be on circular orbits, except for the regions mentioned above. The symmetric drop in rotation curve on both sides of the disk is the strongest argument that we are actually measuring the circular velocity and that this drop is not caused by, for example, a lack of gas on the major axis: an explanation which has been invoked to explain asymmetric drops seen in other edge-on galaxies (Sancisi & Allen 1979).

5. THE DETERMINATION OF THE THICKNESS OF THE HYDROGEN LAYER

In the past, the radial increase of the thickness of the gas layer of external galaxies has been determined from apparent width measurements of the edge channels only (Sancisi & Allen 1979; van der Kruit 1981; Rupen 1991a). The main advantage of this procedure is that the edge channels select a region (the “emitting region”) around the major axis which is relatively narrow, so that its width, as projected onto the sky, does not contribute much to the observed apparent thickness. This procedure has two disadvantages however: 1) the magnitude of the projection effect depends strongly upon inclination, e.g., at $i=85^\circ$ it varies

by a factor of two for an inclination difference of 2° , and 2) only two points per galactocentric radius, one on the approaching side and one on the receding side, are measured.

Irwin & Seaquist (1991) modeled the entire spectral line cube obtained for NGC 3079 to obtain the rotation curve, surface density distribution and gas layer width (assumed to be constant with radius). Braun (1991) devised a technique to determine the inclination and the thickness of the gas layer for M31, where the H I emission is found primarily in the spiral arms. The technique presented here works best if the H I is distributed smoothly.

Below I describe a new technique to simultaneously determine the radial variation of the inclination and the thickness of the gas layer of external galaxies. As the essence of this method is to utilize data from many azimuths (channels), both disadvantages of the edge-channel procedure are circumvented. This is accomplished by modeling the contribution of the emitting region to the apparent width. Two aspects are crucial: 1) the emitting region can be well modelled if the rotation curve is known, for example for a flat rotation curve a channel of a several km s^{-1} wide is sensitive to gas in a wedge-like region in the plane of the galaxy (Sancisi & Allen 1979, their Fig. 6), where the width of this emitting region follows directly from the rotation curve, the observing velocity and velocity resolution, and 2) for a given galactocentric radius the planar width of the emitting region varies systematically with azimuth (i.e., observing frequency, or velocity). Thus the projected width of the emitting region also varies systematically with azimuth and radius in a manner which can be described exactly for a given observed rotation curve and channel width. These projection effects can be clearly seen in Fig. 8 of Sancisi & Allen, where the apparent width of the gas layer is larger in those channels whose velocities are closer to the systemic velocity. The apparent width of the gas layer is then the sum of the projected vertical

thickness of the gas layer and the projected planar width of the emitting region. Only two unknowns (the vertical thickness and the inclination) are involved. Since the apparent widths can be measured at many azimuths, and the planar width of the emitting region can be calculated as a function of galactocentric radius and azimuth, the inclination and vertical thickness of the gas layer can be simultaneously determined from measurements of the apparent thickness in many channels.

5.1. Outline of the Procedure

The procedure outlined below works for a more realistic situation where the rotation curve is not flat and where the gaseous velocity dispersion softens the edges of the wedges. A more detailed description is given elsewhere (Olling 1995b), and is applied in the next subsection.

In the case where a galaxy is not edge-on, the azimuthal dependence of the flaring might be determined from measurements of the apparent thickness (in a given velocity channel) along an ellipse with axial ratio $1/\cos i$. For a close to edge-on galaxy this procedure is difficult, while at $i = 90^\circ$ it fails altogether. However, at any inclination, the galactocentric radius (R) can be determined from the rotation curve ($V_{\text{rot}}(R)$), the major axis position (x) and the observing velocity (V_{chan}):

$$\begin{aligned} R &= \frac{x}{\cos \theta} = x \frac{V_{\text{rot}}(R) \sin i(R)}{|V_{\text{chan}} - V_{\text{sys}}|} \\ &= x \frac{V_{\text{proj}}(R)}{|V_{\text{chan}} - V_{\text{sys}}|}, \end{aligned} \quad (3)$$

with $i(R)$ the inclination, and V_{sys} the galaxy's systemic velocity. Here the assumption is made that the galaxy can be described adequately by a tilted ring model (Rogstad *et al.* 1974; Begeman 1989) which implies that the warp angle ($i(R)$) does not depend on azimuth. It is important to realize that the determination of R depends on the *projected* rotation speed (i.e. the *product*

of $V_{\text{rot}}(R)$ and $\sin i(R)$ which is, at any inclination, much better determined than the individual quantities (Begeman 1989): the kinematic determination of R is robust⁶. When the apparent widths in a given channel are determined, Eq. (3) is used to assign a galactocentric radius to the measurements obtained at major axis position x . For a given channel and major axis position, the planar width of the emitting region can be determined as well, so that the apparent width measurements can be corrected for inclination and projection effects to yield the intrinsic thickness of the gas layer. Below I describe in detail how the width of the planar emitting region as well as the inclination and thickness of the gas layer can be determined.

Rather than using the wedge-approximation discussed in previous sections, I include the effects of the velocity dispersion of the gas, the exact shape of the rotation curve, and the gaseous surface density distribution to determine the planar width of the emitting region. Given these parameters it is easy to calculate, for all points in the galaxy (x, y) , what fraction of the total column density ($\Sigma(R)$) can be detected when observing the galaxy at inclination $i(R)$ and velocity⁷ V_{chan} (Olling 1995b, Chapt. 4). These channel surface density distributions (CSDDs) form a three dimensional data set ($\Sigma(x, y, V_{\text{chan}})$), where each plane represents the face-on surface density distribution which has (given the galaxian properties and the observing geometry) the right radial velocity to be observed in the channel centered on V_{chan} . If observed face-on for example, the emission observed in each channel is a fraction (which depends on the gaseous velocity dispersion and the channel response function, but is constant across the galaxy) of the surface density. Some CSDD maps are presented in Fig. 10. Alternatively, one could think of a CSDD as a

deprojected (to face-on view) channel map of an infinitely thin gas layer. A rough idea about the shape of the CSDDs can be formed by deprojecting (to face-on view) a velocity field which is contoured at $MAX(\Delta V_{\text{chan}}, \sigma_{\text{gas}})$ km s⁻¹ intervals and selecting the area between two contours (with ΔV_{chan} the width of the channels). But note that a CSDD is neither a deprojected channel map nor a deprojected velocity field. Along a line perpendicular to the major axis, the shape of the emitting region is no longer discontinuous, but can be parameterized, to reasonable accuracy, by two Gaussians:

$$\Sigma_C(y; x, V_{\text{chan}}) \propto \left(e^{-\frac{1}{2}((y-Y_C)/W_C)^2} + e^{-\frac{1}{2}((y+Y_C)/W_C)^2} \right), \quad (4)$$

one for the near side and one for the far side. Non-linear least squares fits to the profiles extracted from Fig. 10 yield typical errors of 0.5% - 1.5% and 0.2% - 0.6% for W_C and Y_C , respectively. As the CSDDs are different for each channel, so are (for a given galactocentric radius) Y_C and W_C , which depend mainly on the rotation curve and the gaseous velocity dispersion, respectively. Projecting the CSDD onto the sky, the apparent planar width is given by:

$$\cos i \text{ FWHM}_p(x; V_{\text{chan}}) \approx 2.35 \cos i \times \sqrt{W_C^2(x; V_{\text{chan}}) + [Y_C(x; V_{\text{chan}})]^2}, \quad (5)$$

where the Y_C -term is only included when the projections of the near and far side of the CSDD are unresolved by the beam, i.e. in nearly edge-on viewing geometry. Since the vertical density distribution of the gas is approximately Gaussian (Paper I), and the planar distribution of the CSDD resembles a double Gaussian (Eq. [4]), the line-of-sight integration through this density distribution is approximately double Gaussian as well. In nearly edge-on geometry the two Gaussians merge (the butterfly ‘closes its wings’). The observable width, convolved with the synthesized

⁶The effects of non-circular motions are discussed in Appendix C..

⁷The Channel Response Function appropriate for these VLA observations is used (see Appendix A.).

beam ($FWHM_b$), is given by:

$$FWHM_{\text{obs}}^2(R; V_{\text{chan}}) = FWHM_b^2 + [FWHM_z(R) \sin i(R)]^2 + [FWHM_p(R; V_{\text{chan}}) \cos i(R)]^2, \quad (6)$$

Using this equation, a fit to the measured apparent widths in many channels yields the intrinsic thickness and the inclination of the gas layer. The required values for $FWHM_p(R; V_{\text{chan}})$ are determined from the CSDD maps. In each channel map (and CSDD map) a major axis position is chosen such that galactocentric radius R is sampled [via Eq. (3)]. I solve Eq. (6) using a non-linear least squares technique⁸ which also yields the errors on i and $FWHM_z$. For the case of NGC 4244, typically 12 determinations of $FWHM_{\text{obs}}(R)$ are used. The square of the difference between the observed and model widths is minimized by varying the inclination and gaseous width, where each data point is weighed by the square of the inverse of its error. The error on each data point is calculated by adding (in quadrature) the error in the right-hand side of Eq. (6), as calculated from the errors in i and $FWHM_p$, to the observational error. Since the contribution from the right-hand side depends on the exact value of the inclination, several iterations are required.

Previous workers (Sancisi & Allen 1979; van der Kruit 1981; Rupen 1991a) corrected their edge channel flaring determinations for some of these projection effects, but made no effort to model the emission in lower velocity channels in detail. However, as shown above, the mea-

⁸ The performance of a least squares technique can be greatly improved by imposing physical limits on the fitted parameters. For example I restrict the inclination to lie in the range 0° - 90° , and the thickness of the gas layer to be positive. A standard LSQ routine (e.g. MRQMIN, Press *et al.* 1990) can be easily modified to include physical limits in the step where a new guess for the solution is calculated: if the new guess exceeds a physical boundary, then the new guess is placed halfway between the old guess and the physical boundary.

sured apparent widths in the lower velocity channels provide enough additional information to simultaneously determine the flaring and inclination. Furthermore, since many azimuths (channels) are used, the effects of local irregularities are reduced.

For less inclined systems, inclination and thickness can be determined from each channel individually using

$$\cos i(R; V_{\text{chan}}) = \frac{\Delta d(R; V_{\text{chan}})}{2Y_C(R; V_{\text{chan}})}, \quad (7)$$

and

$$FWHM_z^2(R; V_{\text{chan}}) = \frac{1}{\sin^2 i(R)} \times (FWHM_{\text{obs}}^2(R; V_{\text{chan}}) - FWHM_b^2 + [2.35W_C(R; V_{\text{chan}}) \cos i(R)]^2), \quad (8)$$

where Δd is the projected separation of the two “wings” of the “butterfly”. From the inclination and thickness values determined from the individual channels the weighted averages are calculated, where the weights are the inverse of the square of the errors. The errors in the right hand sides of Eqs. (7) and (8) include the errors on d , $FWHM_{\text{obs}}$, Y_C , W_C and i .

Both the intrinsic thickness of the gas layer and the planar width of the CSDD increase approximately linearly with radius: the former because of the $1/R^2$ DM-halo density distribution (Paper I), the latter because in the wedge approximation of the CSDDs the path through this wedge is proportional to R . Simple analytic considerations (Olling & van Gorkom 1995⁹; Olling 1995b, Chapt. 4) indicate that the ratio of these two projected widths depends strongly on inclination and only weakly on the properties of the galaxy. For a typical channel, the projected gas layer width exceeds the projected CSDD width for inclinations larger than about 60 degrees. This inclination cutoff is confirmed

⁹ Notice a typo in their Eq. (4): $\sigma_z(R)$ has to be replaced by $\sigma_z(R) \times R$

using “observations” of simulated galaxies seen at various inclinations (Fig. 11; Olling 1995b, Chapt. 4). Thus it is expected that for galaxies with inclinations exceeding 60° the flaring, and hence the DM-halo flattening, can be determined.

5.2. The Thickness of NGC 4244’s Gas Layer

For all major axis positions (x) the emission profile perpendicular to the major axis are investigated. Gaussian fits to these profiles yield the peak and width (Fig. 12) for all positions. All the thickness measurements presented in this figure, as well as the odd channels in between, are used in the determination of inclination and thickness of the gas layer. The peak of the fitted Gaussians at each radius is plotted in the two outer panels, the apparent thickness in the inner panels. A fit is only performed if there are at least three independent points with a signal to noise ratio ≥ 4 in the profile. The SW-NE asymmetry in the surface density profile (Fig. 6) at 5.5 kpc and 6-8 kpc can be seen in many of the individual channels, indicating that the SW-NE asymmetry of the radial surface density distribution as determined using the Abel-inversion technique extends over a large range in azimuth.

Because inclination and thickness are calculated rather differently in the nearly edge-on case [Eq. (6)] and the not edge-on case [compare Eqs. (7) and (8)], stringent criteria are applied to avoid spurious two-component fits. A reliable two-component fit must satisfy the following criteria: a) the amplitudes of the components may not differ by more than 60%, b) the components must have equal widths, c) the separation between the components must exceed $MAX(FWHM_b, 0.77 \times FWHM_{cmp})$, and d) its goodness of fit must exceed the goodness of fit of the one-component fit. Generally, the profiles are well represented by a single Gaussian, so that, the thickness and inclination are determined using Eq. (6). The results are presented,

for the two sides of the galaxy, in Fig. 13. The radial variation of thickness in the upper panel, the inclination in the lower panel. The plot on the left-hand side results if the inclination is a free parameter, while fixing the inclination leads to the thickness determinations plotted on the right.

Using the observational errors only, the reduced χ^2 values of the fits [to Eq. (6)] are of the order of $3.5 (\pm 1.5)$ for radii smaller than ~ 8 kpc and increase sharply to $\sim 13 (\pm 7)$ beyond, indicating that either the model is bad or that the errors have been underestimated. In Appendix C. I show that non-circular motions contribute to the error budget of Eq. (6) as well. The inclusion of errors associated with non-circular motions (~ 2 km s $^{-1}$ for $R \leq 8.5$ kpc and ~ 8 km s $^{-1}$ beyond) decreases the reduced χ^2 to values around one. The onset of the warp around 8.5 kpc suggests that modest non-circular motions are associated with the warp. Other explanations are possible however: for example the surface density distribution may be strongly asymmetric in azimuth so that the H I emission arises from either near or far side rather than from both sides, or the warp may be asymmetric like the warp of NGC 4565 (Rupen 1991b).

The beamsize corrected widths inferred from the high ($10''$) and intermediate ($38''$) resolution data sets are generally equal to within the errors, which indicates that the width measurements are not hampered by resolution effects. It is likely that the non-circular motions inferred in the inner 5 kpc (Sec. 4.2., Fig. 9), which might result from the “spiral structure” as seen in the H I surface density distribution (Fig. 6), are not limited to the regions close to the major axis. Because the determination of the thickness of the gas layer is less accurate in the presence of non-circular motions¹⁰, it is not advisable to use this

¹⁰In fact, in Appendix C. I show [Eq. (C21)] that the errors in the derived thickness are proportional to the magnitude of the non-circular motions and to the inverse of the rotation speed, which is rising in the inner 5 kpc.

region to draw inferences about the mass-to-light ratio of the stellar disk. The derivation of the halo’s flattening, which uses the flaring data beyond 8 kpc, is not affected.

Another problem area may be the 7 - 8.5 kpc hump on the south-western side, where the thickness of the gas layer is 70% larger, and the gaseous surface density distribution (Fig. 6) 50% lower than on the north-eastern side. This region is adjacent to a region where the stellar surface density is possibly depressed a factor of ten (Sec. 2. and Fig. 2). In the outer part of the optical disk the self-gravity of the gas can contribute significantly to the vertical force (see Paper I, Fig. 10). In the case of NGC 4244, models which include the gaseous self-gravity have gas layer widths 50% smaller than models which do not, between 6 and 10 kpc. Therefore I plot the north-eastern rather than the average values in the final flaring curve (Fig. 14) from 6 to 8.5 kpc.

From these flaring measurements taken at different resolutions and sensitivities I extract two flaring curves, one for the varying inclination case, the other for the fixed inclination case (Fig. 14). For radii between 6 and 10 kpc I use the flaring data extracted from a 357-pc resolution data set. The high (177 pc) and intermediate (665 pc) resolution flaring results are used for the regions smaller than six and larger than ten kpc, respectively. The “errors” are either the weighted error on the average of the two sides, or if larger, half the difference between the two values, so that the *systematic* differences are reflected by the extent of the error bars.

5.3. Inclination effects

Because the inferred short-to-long axis ratio of the halo is proportional to the square of the true width of the gas layer (Paper I, Paper III), the thickness of the gas layer has to be measured reliably. It must be stressed that the inclination is a critical parameter for determining the intrinsic thickness of the gas layer. This is so because, at

inclinations around 85° a large part of the apparent width arises due to the projected separation of the CSDD wings (Sec. 5.1.), which changes by 40% between 85° and 83° . At these inclinations the DM-halo shape can be determined reliably only if the inclination is accurately known (Paper III).

5.4. Non-circular Motions

The assumption of circular orbits is basic to the thickness determination technique presented in this paper. Closed orbits of ellipticity $\epsilon_{\phi,p}$ exist in elliptic logarithmic potentials, for which the radial and tangential velocity can be found analytically [e.g., Rix & Zaritsky 1995, their Eqs. (7) and (8)]. As a result, the difference between the observable *recession* velocities of an elliptical disk and a circular disk have a period of $\pi/3$ and an amplitude of $\epsilon_{\phi,p}V_{\text{rot}}$. With θ_ϕ the direction of the major axis of the potential, the observable velocity difference between two points at (R, θ) and $(R, -\theta)$ equals zero and $(2\epsilon_{\phi,p}V_{\text{rot}} \sin(2\theta) \sin(\theta + 2\theta_\phi))$ for a round disk and an elliptical disk, respectively. For ellipticities as reported by Rix & Zaritsky ($0.045^{+0.03}_{-0.02}$), the effects of elliptical orbits are smaller than 9 km s^{-1} , so that the shape of the CSDD maps, and hence the determination of the flaring is not affected much. The recession velocity at the major axis equals $V_{\text{sys}} \pm V_{\text{rot}}(R) \{1 + \epsilon_{\phi,p} \cos(2\theta_\phi)\}$. Given the predicted and measured upper limits to $\epsilon_{\phi,p}$, (≤ 0.1 , Dubinski 1994; and ≤ 0.075 , Rix & Zaritsky 1995), the measured 15% decrease in rotation speed cannot be explained by a rapid radial variation in ellipticity or location of major axis of the dark matter distribution.

6. DISCUSSION

The thickness of the gas layer has been measured for only a few galaxies: The Milky Way (e.g., Kulkarni *et al.* 1982; Knapp 1987; Wouterloot *et al.* 1990; Diplas & Savage 1991; Merrifield 1992; Malhotra 1994, 1995), NGC 891

(Sancisi & Allen 1979; van der Kruit 1981; Rupen 1981a), NGC 4565 (Rupen 1991a), and M31 (Braun 1991). The rapid variations (up and down by a factor of 2 - 4 within 500 pc) in the thickness of the gas layer of NGC 891 (Rupen 1991a) and the 7-kpc hump found in the flaring curve of NGC 4244 (Fig. 14) are probably caused by spiral arm streaming motions which change the shape of the emitting regions of the channels (see also Appendix 15). Inside the stellar disks, the thickness ($FWHM$) of the gas layer increases gradually from ~ 150 pc to ~ 800 pc at the edge of the stellar disk, similar to the flaring of NGC 4244 as determined in this paper.

Inside the optical disk ($R \leq 10$ kpc), the radial variation of the dispersion is quite similar to that observed in other, more face-on, systems (van der Kruit & Shostak 1982; Dickey *et al.* 1990; see Kamphuis 1993, Chap. 12, for a review). Beyond the optical disk ($R > 10$ kpc), σ_{gas} increases somewhat (from 8.5 to 9.2 km s $^{-1}$), similar to the dispersion increase (from 6 to 8 km s $^{-1}$) seen in NGC 628 (Kamphuis 1993, Chap. 12, Fig. 1). In the other two systems where measurements of the dispersion beyond the optical disk exist, σ_{gas} declines very slowly, to 6 and 7 km s $^{-1}$ (Dickey *et al.* 1990; Kamphuis 1993). Thus, the radial variation of velocity dispersion in the gaseous medium of NGC 4244 is not unusual.

Rather than determining the best fit M/\mathcal{L} and dark-halo's core radius and central density I use the procedure outlined in Paper I to find the range in stellar mass-to-light ratios which yield acceptable fits to the observed rotation curve (the halo's flattening is not a parameter in this procedure). I then calculate the reduced χ^2 values on a grid which covers this range in M/\mathcal{L} . Recall that for given observed rotation speeds at $2.3h_R$ ($V_{\text{rot}}(2.3h_R)$) and $8h_R$ ($V_{\text{rot}}(8h_R)$) and a choice for the stellar M/\mathcal{L} the dark halo parameters are uniquely determined (Paper I). However, because measurement errors on the rotation curve, different values values for $V_{\text{rot}}(2.3h_R)$ and $V_{\text{rot}}(8h_R)$ are acceptable. I adopted values which

differ by less than 1- σ from the adopted rotation curve which yield the lowest χ^2 values. In Fig. 15 I present the so found 'best fit' and the $\pm 1-\sigma$ mass models. The mass-to-light ratio is rather well determined ($M/\mathcal{L}_B = 3.71^{+2.6}_{-0.4}$). The upper limit coincides with the maximum-disk value (van Albada & Sancisi 1976), for which the peak of the rotation curve due to the stellar disk equals the observed peak rotation speed.

The shape of the vertical distribution of the stars determines the inferred mass-to-light ratio of the stellar disk (van der Kruit 1988). Using a sech^2 vertical distribution, the inferred mass-to-light ratio is twice larger than when using a vertically exponential distribution (for edge-on galaxies). As the M/\mathcal{L}_B value found here (6.3) for the maximum disk case is about twice as large as typical for a maximum-disk Scd galaxy (Broeils 1992, Chapt. 10) the vertical distribution may be exponential rather than sech^2 . Additional information (e.g., K-band imaging) regarding the vertical structure of the stellar disk is required to determine M/\mathcal{L} more accurately.

Beyond the optical disk, the dynamical mass-to-light ratio increases to a value of $14.9 M_{\odot}/L_{\odot}$ at the last measured point (16 kpc), or half that value for the vertically exponential distribution. Neither value is unusual (Broeils 1992, 1995). Only a small amount of dark matter is present: 1.4 times the luminous mass for the maximum disk case, and 3.6 times the luminous mass for the half-maximum disk case (independent of the vertical distribution). As a result of the limited extend of the measured rotation curve, the dark-halo parameters are ill constrained: to within a factor 50 for the core radius and 900 for the central density.

7. CONCLUSIONS

The rotation curve of the almost edge-on galaxy NGC 4244, determined from high resolution H I spectra, rises slowly to about 100 km s $^{-1}$ at 5 kpc, remains flat till the edge of the optical

disk at 10 kpc and decreases in Keplerian manner till the last measured point at seven optical scale lengths (14 kpc). The mass-to-light ratio of the stellar disk lies between 50% and 100% of the maximum-disk value, the core radius and central density of the dark halo could not be determined.

I developed a new technique to determine inclination and flaring for large H I rich galaxies seen at inclinations larger than about 60° . Kinematic information is used to disentangle flaring and warping. The thickness of NGC 4244's gas layer increases gradually from ~ 400 pc at 2 optical scale lengths to ~ 1.5 kpc at the last measured point.

I like to thank Jacqueline van Gorkom for many valuable suggestions to improve this paper, for guidance in image processing, for advice in bicycle racing, for support and encouragement, and for discussing many interesting aspects of extra galactic astronomy. I would like to thank NRAO and the Kapteyn Astronomical Institute, for their hospitality as well as for their excellent software support. I thank NRAO for the generous allocation of observing time for this project. It was a great pleasure to discuss galactic structure and many aspects of H I observations of galactic disks with Michael Rupen. I thank Juan Uson for discussing various aspects of calibrating VLA data and providing us with the wonderful UV-editing tasks UVLIN and UVMLN. Piet van der Kruit helped me a lot by providing the B-band photometry. I also thank John Hibbard, Mike Merrifield and the referee for an unbiased reading of a previous version of this paper. This research has made use of the NASA/IPAC Extragalactic Database (NED) which is operated by the Jet Propulsion Laboratory, CALTECH, under contract with the National Aeronautics and Space Administration. This work was supported in part through an NSF grant (AST-90-23254 to J. van Gorkom) to Columbia University.

APPENDICES

A. DETERMINING THE ROTATION CURVE AND VELOCITY DISPERSION OF AN EDGE-ON GALAXY

In a manner similar to the tangent-point method employed for the Milky Way (e.g., Burton & Gordon 1978; Celnik *et al.* 1979), the gaseous velocity dispersion and the circular velocity can be derived from the extreme velocity tails of spectra taken on the major-axis of an edge-on galaxy. In this section I investigate how gradients (along the line-of-sight) in surface density, rotation speed and velocity dispersion affect this derivation. Small gradients occur naturally in the azimuthally symmetric galaxy models considered in this paper, while strong gradients can occur near spiral arms. Gradients perpendicular to the line-of-sight, beam smearing, are also addressed.

For a galaxy, in which all gas moves at exactly the circular velocity (V_c), gas on the major axis moves at the local rotation velocity. Other positions have lower projected velocities, V_p [Eq. (3)]. In reality, the velocity dispersion of the gas broadens the sharp cutoff at $V_c(R)$ and moves the peak of maximum emission closer to the systemic velocity. The spectrum, $I(x, V, d; S)$, at a point¹¹ (x, d) on the sky depends on the surface density distribution of the gas, the distribution perpendicular to the plane, the gaseous velocity dispersion, the rotation curve, and the channel response function $S(V'; V, \Delta V)$, defined by Eq. (A4). After summing the data along the minor axis, the dependence on minor axis position and the vertical distribution disappear so that the spectrum (or “XV plot”) is given by:

$$I(x, V; S) = \frac{K}{\sqrt{2\pi}} \int dy \frac{\Sigma(y)}{\sigma(y)} \int dV' S(V'; V, \Delta V) e^{(-\frac{1}{2}[(V' - V_p(y))/\sigma(y)]^2)}, \quad (\text{A1})$$

with K a proportionality constant related to the

¹¹The coordinate system is defined in Sec. 4.1..

choice of units, $y = \sqrt{R^2 - x^2}$, and

$$\begin{aligned} V_p(y) &= V_c(R) \times \frac{x}{\sqrt{x^2 + y^2}} \\ &\approx V_c(x) + \frac{y^2}{2x^2}(ax - V_c(x)) . \end{aligned} \quad (\text{A2})$$

Here $V_c(R) \approx V_c(x) + a(R - x)$, and a the gradient in the rotation curve ($\text{km s}^{-1}/\text{kpc}$). A point somewhere along the line of sight whose projected velocity is $\sigma \text{ km s}^{-1}$ lower than the rotation speed will hardly influence parts of the spectrum at velocities larger than $V_c(x)$. Thus, the spatial integral in Eq. (A1) can be limited to a maximum, $\pm y_{\text{max}}$ so that only gas “close” to the major axis will contribute significantly to the extreme velocity tails (EVTs). Eq. (A2) provides an estimate for y_{max} :

$$y_{\text{max}} \approx x \sqrt{-\frac{2 \sigma(x)}{ax - V_c(x)}} . \quad (\text{A3})$$

For NGC 4244, typical values for $\epsilon_m (= y_{\text{max}}/x)$ decrease from 0.85 at 1 kpc to 0.33 at 12 kpc. The velocity dispersion and the surface density can be expanded around $R = x$ as well: $\sigma(y) \approx \sigma(x) \left(1 + \frac{1}{2} bx\epsilon^2\right)$, and $\Sigma(y) \approx \Sigma(x) + \frac{1}{2} cx\epsilon^2$, where b is the fractional gradient of the velocity dispersion (kpc^{-1}), and c the gradient in surface density ($M_{\odot}\text{pc}^{-2}/\text{kpc}$).

For spectral line data obtained with the VLA which are not Hanning smoothed (as is the case for the observations presented in this paper), a channel of width ΔV , centered at V , is sensitive to emission at other velocities V' as well. The channel response function is given by (Rots 1990):

$$S(V'; V, \Delta V) = \frac{\sin(\pi(V' - V)/\Delta V)}{\pi(V' - V)/\Delta V} . \quad (\text{A4})$$

The strong sidelobes of S are reduced by more than an order of magnitude when integrated over the width of a channel (the 1st, 2nd, 3rd, and 4th channels have an effective sensitivity of 100%, +8.6%, -1.9%, and +0.83%, respectively). Limiting the velocity range (to $\pm \frac{1}{2}\Delta V$) of the second

integral in Eq. (A1) and taking S to be unity over this interval allows for an analytic approximation of $I(x, V; S)$, which can then be used to gauge the importance of line-of-sight gradients of the variables.

Approximating the Gaussian term in Eq. (A1) by a parabola and integrating the spatial integral up to ϵ_m , the spectrum can be written as:

$$\begin{aligned} I(x, V) &\approx \left(\frac{\epsilon_m K \Delta V \Sigma}{\sqrt{2\pi\sigma}} \right) e^{-\frac{1}{2}\left(\frac{W}{\sigma}\right)^2} \times \\ &\left\{ 2 - \frac{\epsilon_m^2 W V_c}{3\sigma^2} + \frac{x\epsilon_m^2}{3} \times \right. \\ &\left. \left[\left(\frac{aW}{\sigma^2} \right) + b \left(\frac{W^2}{\sigma^2} - 1 \right) + \frac{c}{\Sigma} \right] \right\} , \end{aligned} \quad (\text{A5})$$

where all galaxian properties are evaluated at radius $R = x$, and with $W = V - V_c(x)$. The multiplicative term in Eq. (A5) is a Gaussian function of dispersion σ . The first term within the curly brackets results from material on the major axis, the second term arises due to material close to the major axis, while the last three terms originate due to radial gradients in rotation speed, dispersion and surface density, respectively. Except in the inner 6 kpc, where beam smearing is important as well, Eq. (A5) represents the measured EVT well. A beam smearing correction could be obtained by from an approximation of the convolution of the spectrum (A5) with the beam. However, as this leads to quite ugly equations, another approach is followed. As we have seen above, the EVT of an XV plot contain information about the intrinsic rotation curve and velocity dispersion. A Gaussian fit to such an EVT yield a value for the position and width of this Gaussian¹². Line-of-sight and beam smearing effects cause these values to deviate from the

¹²In practice multiple components are fitted to the full spectrum such that the EVT is dominated by one component. Because of the additional components (more degrees of freedom) the errors are overestimated. The AIPS tasks SLICE and SLFIT were used to perform the Gaussian fits. However, the version of these tasks which are part of the standard AIPS release re-sample every slice to a 512

intrinsic rotation speed and velocity dispersion. The magnitude of these deviations can be empirically found by comparing the values obtained from fits to a simulated¹³ XV plot with the parameters used in the calculation of the simulated XV plot. I find:

$$\sigma_{\text{gas}} \approx \frac{\sigma_{\text{XV};10}}{(0.9 + \exp[-R/4])} \quad (\text{A6})$$

$$\sigma_{\text{gas}} \approx \frac{\sigma_{\text{XV};38,55}}{(0.9 \exp[-2.5] + \exp[(R - 10)/17])}, \quad (\text{A7})$$

for ($R \leq 10\text{kpc}$) and ($R > 10\text{kpc}$) respectively. The subscripts “10”, “38”, and “55” refer to the beamsize of the data set for which the correction is appropriate. The “XV” subscript refers to the value as fitted to the extreme velocity envelope of the XV plot. Note that the true gaseous velocity dispersion is always smaller than the dispersion of the extreme velocity envelope. As these corrections depend on the input parameters (e.g., beam smearing is insignificant for a flat rotation curve), the input parameters for the calculation of the simulated XV plot should be close to the intrinsic rotation and dispersion curves: this problem is solved by iterating several times. An estimate of σ_{XV} can also be obtained by counting the number ($N_{0,P}$) of velocity channels between the zero and peak emission level of the EVT. This estimate is calibrated by generating Gaussian distributions with a range of dispersions centered at various locations within a velocity channel: ($\sigma_{\text{XV}} = (2.4N_{0,P} - 0.6 \pm 1) \times \frac{\Delta V_{\text{chan}}}{5.2} \text{ km s}^{-1}$). Since $N_{0,P}$ as determined from the data is generally equal to the value determined from the best-fit simulated XV plot, I conclude that the velocity dispersion (and rotation curve, see below) as determined from the Gaussian-fit method is reliable.

Because these relations depend on beam size, channel width, surface density distribution, and

grid, as a result of which the calculated errors are meaningless. I therefore wrote special versions of SLICE and SLFIT which do not re-sample the data.

¹³Using the procedure outlined in Appendix B.

the rotation curve, these relations are specific to the observations of NGC 4244 presented in this paper. The errors, 3σ , about 20% and 5% in the inner and outer part of the galaxy, are largest in those regions with strong surface density gradients.

The corrections required to determine the rotation curve from the XV-plots are given by:

$$V_{\text{rot};10}(R) \approx V_{\text{XV};10} + (1.3 \times \exp[-R/4.0] + 0.35) \times \sigma_{\text{XV};10} \quad (\text{A8})$$

$$V_{\text{rot};38,55}(R) \approx V_{\text{XV};38,55} + (1.0 \times \exp[-R/4.0] + 0.35) \times \sigma_{\text{XV};38,55}. \quad (\text{A9})$$

In regions where the surface density changes rapidly, the smearing correction is least reliable: differences between input and output rotation curves of order 3 - 5 km s^{-1} occur in the inner 5 kpc of the simulated XV plots.

These correction are then applied to the fitted rotation and dispersion values obtained from the data. The resulting dispersion and rotation curves are shown in Figs. 8 and 9, respectively. At some locations, the data EVTs are very different from the simulated EVTs, while adjacent positions have similar EVTs: these locations are likely to be affected by local irregularities and have been discarded.

This procedure does not work perfectly, not even for the azimuthally symmetric model galaxy used here. Both the XV-derived rotation curve and the XV-derived dispersion curves (after applying the corrections specified above) deviate systematically from the input curves. Between 1 and 2 kpc and between 4.5 and 5 kpc the XV-derived rotation curve falls $\sim 8 \text{ km s}^{-1}$ ($\sim 12\%$) and $\sim 3 \text{ km s}^{-1}$ ($\sim 3\%$) below the input curve. These negative differences can be clearly attributed to the strong density enhancements at slightly larger radii, which are thus seen at lower projected velocities: on the “inside” of strong H I density enhancements the XV-velocities are decreased and the true rota-

tion speeds are underestimated. Too large a rotation speed (3 km s^{-1}) is derived in the region where the H I distribution strongly peaks (Fig. 6), between 3.5 and 4.5 kpc. This H I peak behaves like an δ function on the major axis, in which case the XV-velocity directly corresponds to the rotation speed: applying the dispersion correction [Eq. (A8)] thus leads to an overestimate of the rotation speed. In determining the rotation curve of NGC 4244 (§4.2.) I have not tried to compensate for the surface density effects in detail since these H I density peaks may well be spiral arms, in which case the derived rotation speeds may include some spiral arm streaming motions as well. Instead I have followed the upper envelope of both sides and in the regions where the model calculations indicate that too low a rotation speed is inferred from the XV-plots I increased the adopted rotation curve such that is a smooth junction of the adjacent regions. Here the errors are accordingly increased.

Because beam smearing effects are not important beyond 6 kpc, Eq. (A5) can be used to investigate the dependence of the shape of the EVTs on gradients in $V_c(R)$, $\Sigma(R)$, and $\sigma(R)$. Since for a given range in y (or ϵ_m) only a small range in R is sampled, gradients in the rotation curve are unimportant. Gradients along the line of sight in surface density and dispersion cause changes in V_{XV} and σ_{XV} . Using Eqn. (A5) and determining V_{XV} and σ_{XV} as a function of b and c , I find the following offsets (in km s^{-1}):

$$\Delta V_{XV} \approx (-3 \pm 0.7) b \quad , \quad (\text{A10})$$

$$\Delta \sigma_{XV} \approx (1.8 \pm 0.8)b + (0.84 \pm 0.12) \left(\frac{c}{\Sigma} \right) \quad (\text{A11})$$

for ($c \leq 0$), while the c -dependence in (A11) is absent for $c > 0$. Where the Δ -symbol represents the difference between the “no gradients” and the “strong gradients” XV-parameters. Beyond the optical disk, typical values for c/Σ and b are -0.5 and 0.05, respectively. The smearing corrections [Eqs. (A6) through (A9)] take these gradients into account. From Eq. (A11) it follows

that in order to *over* estimate σ_{XV} (and hence σ) large *positive* line of sight gradients in the dispersion are required. With σ_{XV} of the order of 10 km s^{-1} , a 10% over estimate is possible if the dispersion along the line of sight increases to 15 km s^{-1} over a distance of 1 kpc. If such a strong σ -gradient would exist in the radial direction as well, it would certainly be noticed. Very large velocity dispersion gradients have to exist to affect V_{XV} significantly. I conclude that the rotation and velocity dispersion curves can be determined reliably from XV-plots of edge-on galaxies.

B. SIMULATING VLA SPECTRAL LINE OBSERVATIONS

In order to facilitate the interpretation of H I spectral line data I developed software which simulates VLA H I observations of galaxies. The accuracy of the determination of rotation and velocity dispersion curves from XV plots, the beam-smearing corrections, the thickness-and-inclination determination technique, can all be gauged by comparing the “observations” of such a simulated galaxy with the input parameters. Input parameters to this program (VLASIM) are: the observing geometry, $\Sigma(R)$, $V_{\text{rot}}(R)$, and σ_{gas} . The vertical density distribution of the gas layer is calculated employing a physical model for the potential of the galaxy (the multi-component method, Paper I) which yields the gaseous volume density. The rotation speed is assumed¹⁴ to be constant with height above the plane. VLASIM then integrates the amount of hydrogen along lines of sight from the observer through the galaxy, and distributes this amount over the appropriate channels [using the channel sensitivity function Eq. (A4)]. When the line of sight integrations are done, the spectral line cube is smoothed to the requested resolution followed by the addition of realistic noise (if so desired).

¹⁴For several disk-halo models, rotation curves at different z -heights were calculated, all showing that the rotation speed does not vary significantly ($\leq 5\%$) in the region where gas is found ($|z| \leq 3FWHM_{z,\text{gas}}$).

C. THE EFFECTS OF KINEMATICAL DISTORTIONS

As discussed in Sec. 5., knowledge of the rotation curve allows us to determine the intrinsic thickness of the gas layer. However, the technique is sensitive to deviations from the assumed rotation curve. Spiral arm streaming motions of several tens of percent of the rotation speed (several tens km s^{-1}) are not uncommon in spiral galaxies (e.g., Visser 1980; Vogel *et al.* 1988; Boulanger & Viallefond, 1992; Tilanus & Allen, 1993), so that locally the velocity deviates from the circular velocity. When a line of sight is along a spiral arm, there will be a net shift in the radial velocity (type 1), when the line of sight crosses a spiral arm, the radial velocity will not be affected but the dispersion will be larger¹⁵ (type 2). In this section I determine which parts of the galaxy are most susceptible to non-circular motions and present a weighting scheme which minimizes the effects of non-circular motions: a summary is presented in the next section (C.1.).

The galactocentric coordinates $[(x, y, z)$ or $(R, \theta, z)]$ are related to the celestial coordinates $[(x, d)$ centered on the galaxy] in the following way:

$$x = R \cos \theta, \quad (\text{C12})$$

$$d = R \cos i \sin \theta + z \sin i. \quad (\text{C13})$$

where the position angle of the major axis was taken east-west (90°) and where z is the height above the plane. If gas located at $(R, \theta, 0)$ has an excess line of sight velocity of

$$\frac{\Delta V}{\sin i} = [V_{\text{rot}}(R_0) \cos \theta_0 - V_{\text{rot}}(R) \cos(\theta_0 + \Delta\theta)]$$

with respect to a position $(R_0, \theta_0, 0)$, this position will be “seen” in the same channel as $(R_0, \theta_0, 0)$ is. Similarly, a channel $\Delta V \text{ km s}^{-1}$ wide “sees” gas in an area delimited by θ_0 and θ . Expanding $\cos(\theta_0 + \Delta\theta)$ to second order around θ_0 , and

assuming that rotation curve around R_0 is constant, I approximate the above equation and solve for $\Delta\theta$.

$$\frac{\Delta V \csc i}{V_{\text{rot}}(R_0)} \approx \left[\sin \theta_0 \Delta\theta + \frac{1}{2} \cos \theta_0 (\Delta\theta)^2 \right], \quad (\text{C14})$$

and

$$\frac{\Delta\theta}{\tan \theta_0} = \left[-1 + \sqrt{1 + \frac{2\Delta V \csc i \cos \theta_0}{V_{\text{rot}}(R_0) \sin^2 \theta_0}} \right]. \quad (\text{C15})$$

The requirement that the two points $[(R_0, \theta_0, 0)$ and $(R, \theta, 0)]$ have the same major axis distance leads [via Eq. (C12)] to the following relation for $\Delta R (\equiv R - R_0)$:

$$\frac{\Delta R}{R_0} \approx \left(\frac{\Delta\theta}{1 - \Delta\theta \tan \theta_0} \right) \tan \theta_0 \quad (\text{C16})$$

In the lower panel of Figure 16 I present the relations, both practically independent of inclination, for $\Delta\theta$ and ΔR graphically for the case where $\Delta V = 10 \text{ km s}^{-1}$ and $V_{\text{rot}}(R_0) = 100 \text{ km s}^{-1}$. Although this galaxy model is extremely simple, the opening angles as determined for a more realistic model behave similarly: the high velocity channels (small θ_0) are wider than the low velocity channels. For $\theta_0 \leq 50^\circ$ the fractional range in galactocentric radius is small so that the approximate relation for ΔV (C14) is reasonable, whether or not the rotation curve is constant around R_0 .

If the positions (R_0, θ_0, z_0) and $(R, \theta, 0)$ project on the same position on sky, and if due to an excess motion they also have the same velocity, then their positions in the observer’s spectral-line cube will be the same. The equivalent vertical height of this streaming motion (or, equivalently, of a channel $\Delta V \text{ km s}^{-1}$ wide) equals z_0 . Using (C13), (C16) and expanding $\sin(\theta)$ around θ_0 I find:

$$z_0 \approx R_0 \left(\frac{\Delta\theta}{\cos \theta_0 \tan i} \right). \quad (\text{C17})$$

I plotted the projection of $z_0 (\equiv z_0 \sin i)$ in the second to bottom panel of Figure 16. The curves are labeled with the corresponding galactocentric

¹⁵I thank Ron Allen for pointing this out.

radii. For $i = 85^\circ$ its value is small compared to the projected vertical thickness of the gas layer, but its importance relative to the projected vertical thickness of the gas layer grows rapidly with decreasing inclination ($\propto \tan^{-1} i$).

The systematic errors introduced by streaming motions are more easily understood when considering the corresponding planar width of the CSDD, $\Delta Y(\Delta V) \approx R_0 \left(\frac{\Delta \theta}{\cos \theta_0} \right)$, which can be approximated as:

$$\frac{\Delta Y(\Delta V)}{R_0} \approx \left[\cos \theta_0 \left(1.81 \mathcal{V} \sin^{1.2} \theta_0 + \sqrt{\mathcal{V} \cos \theta_0} \right) \right]^{-1}, \quad (\text{C18})$$

with $\mathcal{V} \equiv [(V_{\text{rot}}(R_0) \sin i)/(2\Delta V)]$. In the region close to the major axis, kinematical distortions have an effect proportional to the square root of the fractional velocity deviation (2^{nd} term), in the lower velocity channels the proportionality is approximately linear (1^{st} term). Thus, the channels close to the major and minor axes have long pathlengths through the galactic disk and are hence easily affected by kinematical or surface brightness irregularities (Fig. 16, third panel from below). The edge-channel itself is even wider as the two sides (at $\pm\theta_0$) merge together.

Streaming motions of type 1 cause the centers of the CSDD to shift along the line of sight, typically by $\pm\Delta Y$ [see also Eq. (C20)]. In the almost edge-on situation, the two sides of the CSDD, as projected on the sky, are overlapping so that the projected planar width [Eq. (5)] and its error are dominated by the Y_C term. Visser (1980) presents model velocity fields for M 81 which include spiral arm streaming motions (his Fig. 10). The equivalent CSDD map results after deprojection of the velocity field (see also Sec. 5.1.). From these velocity fields it is clear that the centers of the CSDDs shift substantially due to spiral arm streaming motions: outwards on the outside of the arms and inwards on the inside of the arms. The strong kinks follow the spiral arm and would

produce sudden changes in the separation of the near and far sides of the CSDDs and in the width thereof, over a large range in azimuth. If streaming motions are present, but the resulting CSDD-kinks are not taken into account in the analysis, the inferred widths may show strong gradients when crossing a spiral arm. Such may be the reason for the large thickness gradients seen in NGC 891 (Rupen 1991a) and NGC 4244 (the 7-kpc hump, Sec. 5.2.).

At lower inclinations, when the two sides of the CSDD are separated, streaming motions of type 2 affect the width determination [Eq. (C21)], while the errors on Y (type 1 streaming motions) hamper the determination [via Eq. (7)] of the inclination. This is illustrated in the top panel of Figure 16, where I plot the inclination error resulting from a velocity shift of 10 km s^{-1} :

$$\Delta i \approx \frac{\cos i}{\sin^2 i} \frac{\Delta \theta}{\sin \theta_0 \cos \theta_0}. \quad (\text{C19})$$

Thus, small streaming motions occurring close to either the minor or the major axis can cause large errors in the inferred inclination. Furthermore, the inclination errors are strongly inclination dependent: $\Delta i(i = 65^\circ) \approx 6\Delta i(i = 85^\circ)$.

C.1. Summary

I will use the above determined systematic errors estimates in the thickness & inclination determination process (Sec. 5.1.). The effect of spiral arm streaming motions is to either shift the center of the CSDD along the line of sight or to increase the apparent velocity dispersion, the former having more severe effects. To our advantage, the expected systematic errors scale with the width of a CSDD wing (calculated for a given gaseous velocity dispersion σ_{gas}),

$$\delta Y_C \approx \frac{\Delta Y(\Delta V)}{\Delta Y(\sigma_{\text{gas}})} \times FWHM_C(\sigma_{\text{gas}}), \quad (\text{C20})$$

and

$$\delta FWHM_C \approx \left(\sqrt{1 + \left(\frac{\Delta Y(\Delta V)}{\Delta Y(\sigma_{\text{gas}})} \right)^2} - 1 \right) \times FWHM_C(\sigma_{\text{gas}}), \quad (\text{C21})$$

are easily calculated from the CSDD model maps and Eq. (C18). These systematic errors increase towards lower inclinations and are proportional to $(\sin i \sin \theta \cos \theta)^{-1}$: the regions around both principal axes are most easily affected by streaming motions.

D. OPTICAL DEPTH EFFECTS

In the Milky Way the optical depth in the H I line is substantial within a few degrees from the galactic plane (e.g., Dickey *et al.* 1983). Typically, the total emission along the line of sight is under estimated by 15%. Similar values are found for edge-on external systems (Haynes & Giovanelli 1984). We thus expect similar values for NGC 4244. Braun & Walterbos (1992) estimate that the cold interstellar medium, which is mostly responsible for the absorption (see below), has a volume filling factor of about 1 - 8%, for the Milky Way and M31, respectively. This cold material forms a layer two to three times thinner than the warm H I (e.g., Kulkarni & Heiles 1988; Braun & Walterbos 1992). For NGC 4244, we thus expect that emission profiles perpendicular to the major axis might be affected by absorption on the midplane, resulting in larger apparent widths. However, from the peak surface brightness and apparent width measurements (Fig. 12) such effects are not obvious: profiles with a high peak column density do not seem to be broader. A more detailed, albeit idealized, calculation of the optical depth is given below.

The optical depth in the H I line for a uniform medium of length l and number density n is given by Braun & Walterbos. Their Eq. (7) reads:

$$\tau = 170 \frac{n l}{T_{s,100} \Delta V}, \quad (\text{D22})$$

with $T_{s,100}$ the spin temperature in units of 100 K, and ΔV the width of the channel in km s^{-1} . In Sec. 4. the surface density, the rotation curve and the velocity dispersion were derived assuming low optical depth. Those derived quantities can be used to evaluate the quantities in

Eq. (D22) and check the validity of the assumption of low optical depth. The CSDD maps provide the H I surface density for which the projected velocity equals the observing velocity ($\pm \frac{1}{2} \Delta V$). Investigating these CSDD channel maps (Fig. 10) we find typical peak column densities of 0.5 - 1 $M_{\odot} \text{pc}^{-2}$ per channel for galactocentric radii smaller than 7 kpc, and much less beyond. In edge-on geometry, the surface density distribution along the line of sight is a double Gaussian [Eq. (4)] with a typical width ($FWHM_p$) for each component of 3 ± 1 kpc. The H I volume number density is given by: $n = 5.5 \cdot 10^{-3} (\Sigma_1 / FWHM_{z,1}) \text{ cm}^{-3}$, where the units for surface density and thickness are $M_{\odot} \text{pc}^{-2}$ and kpc. The optical depth can then be rewritten as:

$$\tau = 0.156 \frac{\Sigma_1 FWHM_{p,3}}{FWHM_{z,1} T_{s,100}}, \quad (\text{D23})$$

where a channel width of 6.2 km s^{-1} was used. Typical values for the spin temperature of the cold component of the interstellar medium range from 100 - 175 K (for the Milky Way and M31, respectively; Braun & Walterbos 1992). Smaller values are found in individual clouds (Spitzer 1978, p. 48, and references therein). Taking the model widths as representative for the thickness of the gas layer ($\sim 250 \text{ pc}$, Fig. 14), and assuming that the cold medium fills the entire volume we find $\tau \sim 0.33$ (30% attenuation). If the cold medium is clumpy with a low filling factor, as in the Milky Way, we might expect 3 clouds per kpc with an optical depth ≥ 1 (Kulkarni & Heiles 1988). In an exactly edge-on geometry this density of clouds would correspond to a large optical depth. However, at an inclination of 85° the path through the galaxy ($\sim 3 \text{ kpc}$) corresponds to a change in z of $\sim 260 \text{ pc}$ (about three times the thickness of the cold gas layer), so that the number of absorbing clouds per line of sight is reduced. Because the pathlengths $FWHM_p$ are comparable for all velocity channels, the optical depth effects are comparable in all channels (in the inner 7 kpc).

Beyond 7 kpc the surface densities are much smaller so that optical depth effects are not important in the derivation of the shape of the DM halo (Paper III).

REFERENCES

- Aaronson, M., Bothum, G., Mould, J. R., 1986, *ApJ*, 302, 536
- Albada, T.S., van, Bahcall, J.N., Begeman, K., Sancisi, R., 1985, *ApJ*, 295, 305
- Albada, T.S., van, Sancisi, R., 1986, *Phil. Trans. R. Soc. Lond. A.*, 320, 447
- Begeman, K., 1989, *A&A*, 223, 47
- Bergstrom, J., Gehrz, R.D., and Jones, T.J., 1992, *PASP*, 104, 695
- Bicay, M.D., Helou, G., 1990, *ApJ*, 362, 59
- Binney, J., Tremaine, S., 1987, *Galactic Dynamics*, Princeton University Press
- Binney J., Mamon G.A., 1982, *MNRAS*, 200, 361
- Bosma, A., 1981, *AJ*, 86, 1971
- Botinelli, L., Gouguenheim, Fouqué, P., Paturel, G., 1990 *A&AS*, 82, 391
- Bottema, R., 1989, *A&A*, 221, 249
- Boulanger, F, Viallefond, F., 1992, *A&A*, 266, 37
- Braun, R., 1995, *A&AS*, 114, 409
- Braun, R., 1991, *ApJ*, 372, 54
- Braun, R., Walterbos, R.A.M., 1992, *ApJ*, 386, 120
- Bregman, J.N., Glassgold, A.E., 1982, *ApJ*, 263, 564
- Broeils, A.H., 1995, in *Dark Matter*, edited by S.S. Holt, C.L. Bennet (AIP conference proceedings 336), p. 125
- Broeils, A.H., 1992, Ph. D. Thesis, Rijksuniversiteit Groningen
- Burstein, D., Heiles, C., 1984, *ApJS*, 54, 33
- Burton, B.W., Gordon, M.A., 1978, *A&A*, 63, 7
- Carignan, C., Puche, D., 1990, *AJ*, 100, 394,
- Casertano, S., 1983, *MNRAS*, 203, 735
- Casertano, S., van Gorkom, J. H., 1991, *AJ*, 101, 1231
- Celnik, W., Rohlfs, K., Braunsfurth, E., 1979, *A&A*, 76, 24
- Condon, J.J., 1987, *ApJS*, 65, 485
- Deharveng, J.M., Bixler, J., Joubert, M., Bowyer, S., Malina, R., 1986, *A&A*, 154, 119
- de Vaucouleurs, G., 1975, in *Stars and Stellar Systems*, edited by A. Sandage, M. Sandage, J. Kristian (Chicago Univ. Press), Chapter 14, p 557
- de Vaucouleurs, G., de Vaucouleurs, A., Corwin, H.G., 1976, *Second Reference Catalogue of Bright Galaxies*, Austin, University of Texas Press (RC2)
- Dickey, J.M., Hanson, M.M, Helou, G., 1990, *ApJ*, 352, 522
- Dickey, J.M., Kulkarni, S.R., van Gorkom, J.H., Heiles, C.E., 1983, *ApJS*, 53, 591
- Diplas, A., Savage, B.D., 1991, *ApJ*, 377, 126
- Dubinski, J., 1994, *ApJ*, 431, 617
- Haynes, M. P., Giovanelli, R., 1984, *AJ*, 89, 758
- Huchtmeier, W.K., 1975, *A&A*, 45, 259
- Huchtmeier, W.K., Seiradakis, J.H., 1985, *A&A*, 143, 216
- Hummel, E., Sancisi, R., Ekers, R.D., 1984, *A&A*, 133, 1
- Irwin, J. A., Seaquist, E.R, 1991, *ApJ*, 371, 111
- Kamphuis, J., 1993, Ph.D. Thesis, Rijksuniversiteit Groningen
- Knapp, G.R., 1987, *PASP*, 99, 1134
- Knapp, G.R., Tremaine, S.D., Gunn, J.E., 1978, *AJ*, 83, 1585

- Kraan-Korteweg, R.C., Tammann, G.A., 1979, *Astron. Nachr.*, 300, 181
- Kruit, P.C. van der, 1981, *A&A*, 99, 298
- Kruit, P.C. van der, Searle, L., 1981, *A&A*, 95,105
- Kulkarni, S.R., Heiles, C., 1988, in *Galactic and Extragalactic Radio Astronomy*, edited by G.L. Verschuur and K.I. Kellermann (Springer-Verlag), Chapter 3
- Kulkarni, S.R., Blitz, L., Heiles, C., 1982, *ApJ*, 259, L63
- Lake, G., Feinswog, L., 1989, *AJ*, 98,166
- Malhotra, S., 1994, *ApJ*, 433, 687
- Malhotra, S., 1995, *ApJ*, 448, 138
- Merrifield, M.R., 1992, *AJ*, 103, 1552
- Napier, P.J., Thompson, A. R., Ekers, R. D., 1983, *IEEE Proceedings*, 71, 1295
- Olling, R.P., 1996, *AJ*, Aug. (Paper III, astro-ph/9605111)
- Olling, R.P., 1995, *AJ*, 110, 591, (Paper I, astro-ph/9505002)
- Olling, R.P., 1995b, Ph.D. Thesis, Columbia University, available via anonymous ftp from parsifal.phys.columbia.edu (US) or <http://astro.soton.ac.uk/~olling/PrePrints/Thesis/> (Europe)
- Olling, R.P., van Gorkom, J.H., 1995, in *Dark Matter*, edited by S.S. Holt, C.L. Bennet (AIP conference proceedings 336), p. 121 <http://astro.soton.ac.uk/~olling/PrePrints/ConferenceProceedings/>
- Persic, M., Salucci, P., Stel, F., 1995, submitted to *MNRAS*, astro-ph/9506004
- Press, W.H., Flannery, B.P, Teukolsky, S.A., Vetterling, W.T., 1990, in *Numerical Recipes* (Cambridge University Press)
- Rice, W., 1993, *AJ*, 105, 67
- Rix, H.W., Zaritsky, D., 1995, *ApJ*, 447, 82
- Rogstad, D.H., Lockhart, I.A., Wright, M.C.H., *ApJ*193, 309
- Rots, A., 1980, A short guide for spectral line observers
- Rupen, M.P., 1991a, Ph.D. Thesis, Princeton University
- Rupen, M.P., 1991b, *AJ*, 102, 48
- Sage, L.J., 1993, *A&A*, 272, 123
- Sandage, A., Bedke, J., 1994, in *The Carnegie Atlas of Galaxies* (Carnegie Institution of Washington)
- Sandage, A, Tammann, G.A., 1975, *ApJ*, 196, 313
- Sancisi, R., Allen, R.J., 1979, *A&A*, 74, 73
- Schwarzschild, M., *AJ*, 59, 273
- Schlickeiser, R., Werner, W., Wiebelinski, R., 1984, *A&A*, 140, 277
- Spitzer, L., Jr., *Physical Processes in the Interstellar Medium* (New York, John Wiley and Sons)
- Ternstrup, D.M., Davies, R.L., Frogel, J.A., Depoy, D.L., Wells, L.A., 1994, *ApJ*, 432, 518
- Tilanus, R.P.J., Allen, R.J., 1993, *A&A*, 274, 707
- Visser, H.C.D., 1980, *A&A*, 88, 159
- Vogel, S.N., Kulkarni, S.R., Scoville, N.Z., 1988, *Nature*, 334, 402
- Warmels, R.H., 1988, *A&AS*, 72
- Wouterloot, J.G.A., Brand, J., Burton, W.B., Kwee, K.K., 1990, *A&A*, 230, 21

Fig. 1.— This image of NGC 4244, taken on a IIIaJ-plate, was kindly made available by Piet van der Kruit. See van der Kruit & Searle (1981a) for details. The weak dustlane, barely visible on a TV monitor, could not be reproduced in this greyscale image. The contours ($[2\ 4\ 8\ 16] \times 6 \times 10^{20} \text{ cm}^{-2}$) represent the total H I column densities at a resolution of $10'' \times 10''$ (175x175 pc). A greyscale representation of the total H I map is presented in Fig. 3.

Fig. 2.— In this figure I present four radial light profiles, each again composed of three profiles: SW (dotted line), NE (dashed line), and average (full line). For clarity, the profiles have been offset by a constant C. From top to bottom the profiles are derived from: a) all light ($C=0.69$), b) all light within 420 pc from the major axis ($C=-2.81$), c) all light more than 420 pc “above” (east of) the midplane ($C=-6.31$), and d) all light more than 420 pc “below” (west of) the midplane ($C=-9.81$). Extinction is not important in the determination of the radial scale length (h_R) because all profiles are consistent with the same radially exponential distribution, with $h_R=2.0$ kpc (the filled circles).

Fig. 3.— Two representations of the total H I distribution are shown. A low resolution ($38'' \times 38''$, 665 pc) contour plot is superimposed on a high resolution ($10'' \times 10''$, 175 pc) grey scale image. The image has been rotated counterclockwise by 48° (NE is up, SW is down). The units for the contours (0.1 0.4 0.8 1.6 3.2 6.4 12.8) and the greyscales are 10^{20} cm^{-2} . A tickmark along the vertical axis, $1'$, corresponds to roughly 1 kpc. The slight warp sets in around 9 arcmin, the edge of the optical disk. Clear features in the high resolution image are the the high surface brightness peaks seen on both sides located approximately 6 arcmin from the center. Notice an approximately 2 kpc diameter region of low column densities, extending from about +3 to +5 kpc. The edges of this feature seem to extend to larger height above the plane. This feature is also clearly visible in the channel maps (Fig. 5).

Fig. 4.— The Global Profile, or the total H I flux as a function of velocity, determined from the $55'' \times 55''$ resolution data set. The systemic velocity is the mean of the 10%, 20% and 50% points, $244.4 \pm 0.4 \text{ km s}^{-1}$. A small asymmetry between the approaching and receding sides can be seen. Typical uncertainties in the flux equal 0.025 Jy/channel.

Fig. 5.— A contour representation of the channel maps at $38'' \times 38''$ (665 pc) resolution superposed on a greyscale image of the channel maps at $28.3'' \times 10.1''$, (495x177 pc) resolution. The greyscale levels correspond to column densities of $[1\ 1.5\ 3\ 6\ 9] \times 10^{20} \text{ cm}^{-2}$ (the lowest level is $\sim 2.6\sigma$), the line contours to $[-0.07\ 0.07\ 0.1\ 0.2\ 0.4\ 0.8] \times 10^{20} \text{ cm}^{-2}$ (the lowest contour is $\sim 2.5\sigma$). The channels of the approaching and receding sides are combined into one frame. The value printed in the upper left corner indicates the velocity offset from the systemic velocity (i.e., $|V_{\text{chan}} - V_{\text{sys}}| / \Delta V_{\text{chan}}$). In order to visualize the vertical structure better, the horizontal scale is expanded. The orientation is as in Fig. 3, the distances are relative to the pointing center listed in Tab. 2,

Fig. 5b.— The channels which show emission on the receding as well as on the approaching side are shown individually here. The same coding of greyscales and line contours is used as in Fig. 5a .

Fig. 6.— The gaseous surface density calculated using eqn (2, see Sec. 3.1.), on a linear (lower panel) and logarithmic scale (upper panel). The full line, the dotted line, and the dashed line represent the average, the south-western, and the north-eastern surface density profiles. Like in the Milky Way (Knapp *et al.* 1978; Blitz, private communication), no sharp cutoff is observed in the H I distribution.

Fig. 7.— The major-axis velocity (XV) plot of NGC 4244. The lowest five contours are derived from channel maps at low resolution ($55''$), the highest five contours from $10''$ resolution channel maps. All emission within 2.5 kpc from the major axis was summed. The two sides are remarkably similar, both in kinematics and extent (to about 15 kpc or seven optical scale lengths). Only between +3 and +5 arcmin, the north-eastern side shows a marked dip in the XV-plot. This area is readily identified with a lack of gas on the major axis in the channels 18 through 20 (see Figure 5). Note that this hole does not “punch through” the whole disk. The derived rotation curve is indicated by the filled circles.

Fig. 8.— The beam-smearing corrected [using Eqs. (A6) and (A7)] tangential velocity dispersion as derived from the high ($10'' \times 10''$), intermediate ($38'' \times 38''$) and low ($55'' \times 55''$) XV-plots (bottom, middle and top panel respectively). The south-western, north-eastern, and adopted average curves are indicated by the dotted line, the dotted full line and the filled circles respectively. The measurements are consistent with a constant velocity dispersion of roughly 8.5 km/s. The fat horizontal bars in the lower right corners indicate the size of the beam.

Fig. 9.— The beam-smearing and velocity dispersion corrected [using Eqs. (A8) and (A9)] rotation curve for the two sides of the galaxy. For an explanation of the symbols, see Fig. 8.

Fig. 10.— This figure shows a representative set of CSDDs. The channel numbers are shown in the top right corner of each panel. As the CSDDs are symmetric with respect to the major axis (the horizontal axis), only one quadrant is displayed. The vertical axis of each plot represents the distance along the line of sight (LOS axis). The contours represent the effective column density a given channel is sensitive to. In this coordinate system, the observer would be located at $(0, -\infty)$. We clearly recognize the wedge-like structure valid for the simple model galaxy, however, the wedges have become wiggly and curve back towards the major axis (as a result of the declining rotation curve). For channels close to the extreme velocity channel (-19), the gaseous velocity dispersion broadens the wedges significantly, and fills up the gap between the near and far side.

Fig. 11.— The results of simulated VLA H I spectral line observation of a model galaxy like NGC 4244, inclined by 72° . The simulated spectral line cube is processed in the same manner as the observations of NGC 4244. The recovered inclinations are shown in the lower panel, while the recovered widths are presented in the top panel. The filled circles represent the input model widths. No noise was added to the simulated spectral line cube.

Fig. 12.— In this figure the results of the Gaussian fits to the channel maps are presented. The middle two panels show the measured widths ($FWHM$, beam size corrected, in units of kpc), the outer two panels show the fitted peaks ($M_{\odot}\text{pc}^{-2}$, beam size corrected). The results obtained from the ($10''.1 \times 28''.3$, 177×495 pc) channel maps are represented by the open squares, the fits to the intermediate resolution ($38''$, 665 pc) maps by the full line (with error bars). At few positions two component fits could be made, these are indicated by filled symbols (filled triangles for the intermediate resolution data). The two left-hand panels are determined from the south-western side, the two right-hand panels from the north-eastern side.

Fig. 13.— Here I present the thickness (upper panel) and inclination (lower panel) derived from the fitted widths (at $10''.1$ resolution) presented in Fig. 12 using the procedure described in Sec. 5.1.. Both sides (south-western part on the left) of the galaxy are shown. The fat bar in the lower left corner of the top panel represents the size of the beam, horizontally and vertically for the major axis and minor axis, respectively. For the panels on the left hand side I allowed the inclination to vary, the panels on the right hand side are calculated with a fixed inclination of 84.5° . The filled circles represent the average of both sides. The weighting scheme which takes potential errors due to streaming motions into account was used (see Appendix C.).

Fig. 13b.— Thickness and inclination as derived from the $38'' \times 38''$ resolution channel maps.

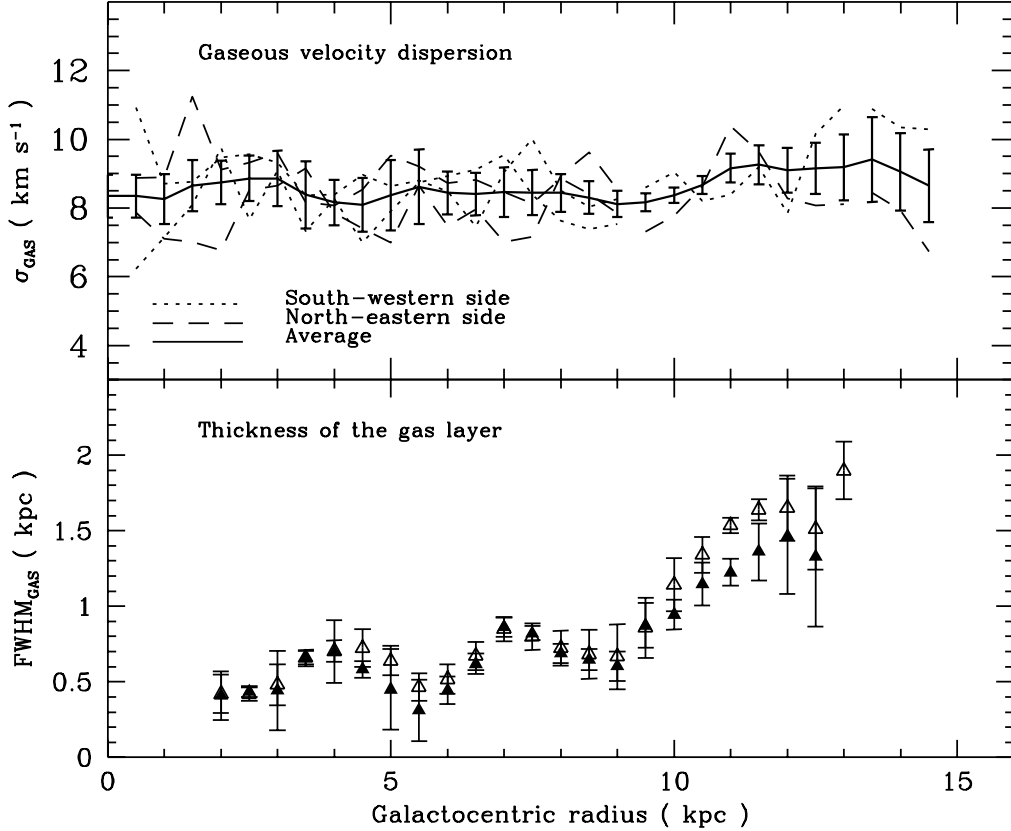


Fig. 14.— The lower panel shows the measured widths (open and filled triangles with error bars, for the fixed and varying inclination case, respectively). The observed flaring curve is the average of the north-eastern and south-western sides, except in the 6.5 - 9 kpc region, where the north-eastern flaring data are used (see Sec. 4.2.) The 7 kpc hump is probably caused by spiral arm streaming motions (Appendix 15). The top panel displays the velocity dispersion measurements (full line with error bars). The dotted lines are determined from the south-western side, the dashed lines from the north-eastern side ($10''$ and $38''$, for $R \leq 9$ kpc; $38''$ for $R \in (9, 13]$ kpc, and $55''$ beyond). The adopted dispersion curve (full line with error bars) is the weighted average of these individual curves.

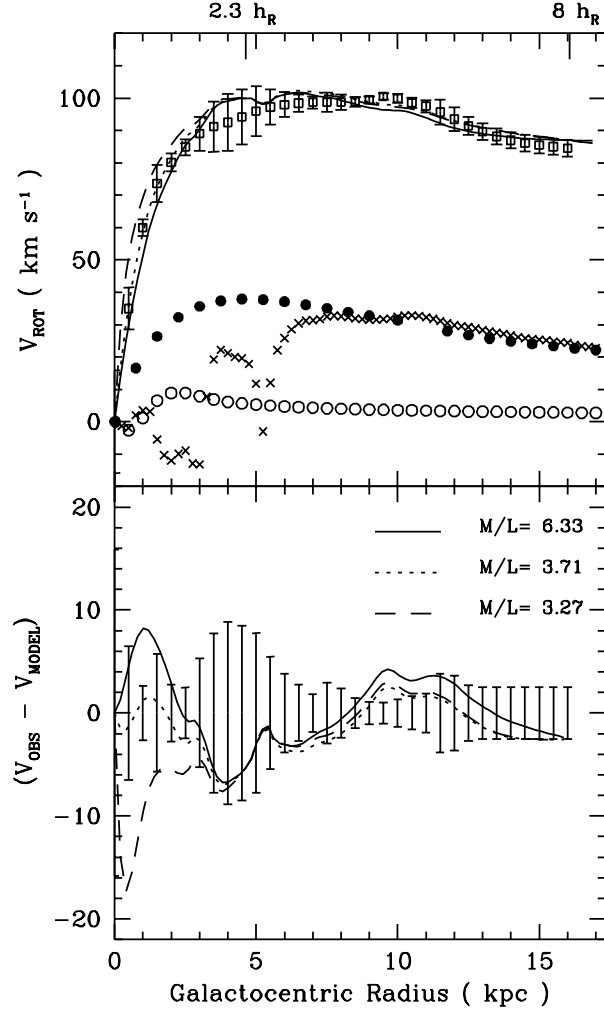


Fig. 15.— The top panel shows disk-halo decompositions of the observed rotation curve (squares with error bars) into components due to the gaseous disks (H I, crosses; H₂, open circles), a component due to the stellar disk (vertically sech² and radially exponential till $R_{\text{max}}=10$ kpc, $M/\mathcal{L}_B=1$; filled circles) and a DM component. The individual contributing DM components are not shown. The data points are independent out to 13 kpc, beyond the resolution equals 1 kpc. The rotation values at $2.3h_R$ and $8h_R$ are differ slightly (100 and 87 km s⁻¹) from the adopted rotation curve (Fig. 9) such as to minimize the residuals (lower panel), see text. The three disk-halo decompositions ($[M/\mathcal{L}_B = 6.33, R_c = 13$ kpc, $\rho_{h,0} = 1.43$ m $M_\odot/\text{pc}^3]$ full line, $[M/\mathcal{L}_B = 3.71, R_c = 0.65, \rho_{h,0} = 233]$ dotted line, $[M/\mathcal{L}_B = 3.27, R_c = 0.28, \rho_{h,0} = 1300]$ dashed line) represent the best fit ($M/\mathcal{L}_B = 3.71, \chi^2=0.864$, 32 degrees of freedom) and those models with a reduced χ^2 value 1.0 larger. For the disk-halo decompositions presented here, the f_m , f_8 , and β_8 parameters (as defined in Paper I) have the values 0.7094, 0.6033, and 0.861 respectively.

Fig. 16.— This figure illustrates the possible effects of streaming motions on the apparent widths (see Appendix C.). All curves presented scale roughly linearly with the ratio of streaming motion and circular speed. For CSDDs centered on θ_0 , I plot the angular width (the lowest panel, crosses) and the normalized range in radius (filled circles) which corresponds to a streaming motion of magnitude $\Delta V \text{ km s}^{-1}$. The corresponding apparent width on the sky is plotted in the one but lowest panel. In the second panel from the top, I plot the linear distance, in the plane of the galaxy, that the angle $\Delta\theta$ corresponds to. Close to the major and minor axes, long pathlengths reflect a strong sensitivity to small streaming motions. The inclination errors resulting from such streaming motions are plotted in the top panel.

Table 1: Optical parameters

Distance		3.6 Mpc
B-band radial scale length	$h_{R,B}$	2.0 kpc
B-band vertical scale height exponential	$z_e (= \frac{1}{2} z_0)$	0.21 kpc
edge of optical disk	$R_{\max,SW}$	10.0 kpc
	$R_{\max,NE}$	8.0 kpc
face-on central surface brightness	$\mu_{0,B}$	$22.4 \pm 0.07 \text{ mag arcsec}^{-2}$
	$L_B(0)$	$74.6 \pm 5 L_\odot \text{ pc}^{-2}$
diameter of $25 \text{ mag arcsec}^{-2}$ isophote	D_{25}^i	11 kpc
total B-band luminosity	$L_{\text{tot},B}$	$1.8 \cdot 10^9 L_\odot$, $M_B = -17.7$

Note: No correction for galactic extinction was required ($E(B-V)=0$; Burstein & Heiles 1984). The subscript “B” refers to the value as determined from B-band photometry. The face-on central surface brightness is calculated *assuming* a $\text{sech}^2(z/z_0)$ vertical light distribution. For a distribution which is exponential in the vertical direction, $L(0)$ is twice larger. The absolute magnitude, the central surface brightness, and the total luminosity, which are derived from the central surface brightness and $h_{R,B}$, change accordingly (to $21.6 \text{ mag arcsec}^{-2}$, $149 L_\odot \text{ pc}^{-2}$ and $M_B = -18.4$, respectively). Note that D_{25}^i -values derived from the sech^2 and exponential luminosity density distributions (9.6 and 12.6 kpc) bracket the statistically corrected RC2 value (de Vaucouleurs *et al.* 1976).

Table 2: Instrumental parameters for the VLA observations of NGC 4244

Observing dates	2 May 1989, B-array, 6 hours on source 30 Nov 1989, D-array, 15 min on source 29 Nov 1990, C-array, 45 min on source 21 Aug 1992, D-array, 7 hours on source
Pointing center	12 ^h 14 ^m 59 ^s .9 38° 5' 6".0
Velocity of band center	245 km s ⁻¹ , heliocentric, optical definition
Number of channels	63
channel separation	5.2 km s ⁻¹
Velocity resolution	6.2 km s ⁻¹
map making characteristics	beam sizes: along and \perp to the major axis
10".0 x 10".0	B + C + D-array, uniformly weighted, tapered
28".3 x 10".1	B + C + D-array, uniformly weighted, tapered
38".0 x 38".0	B + C + D-array, naturally weighted
55".0 x 55".0	1992 D-array, naturally weighted
rms noise in channel maps	
10".0 x 10".0	2.3 mJy beam ⁻¹ \rightarrow 131 10 ¹⁸ cm ⁻²
28".3 x 10".1	1.9 mJy beam ⁻¹ \rightarrow 39 10 ¹⁸ cm ⁻²
38".0 x 38".0	0.73 mJy beam ⁻¹ \rightarrow 2.8 10 ¹⁸ cm ⁻²
55".0 x 55".0	0.76 mJy beam ⁻¹ \rightarrow 1.4 10 ¹⁸ cm ⁻²

Table 3: Parameters derived from the H I distribution

$\alpha_{\text{adopted}}(1950)$	12 ^h 14 ^m 59 ^s .9
$\delta_{\text{adopted}}(1950)$	38° 4' 59".7
Position angle	-48°
Inclination	\sim 84°5
$R_{\text{H I}}$	11.0 kpc
V_{sys} , heliocentric	244.4 ± 0.3 km s ⁻¹
$M_{\text{tot,H I}}$	$(1.34 \pm 0.07) 10^9 M_{\odot}$
$M_{\text{tot,H I}} / L_B$	$0.74 M_{\odot} L_{\odot}^{-1}$
W_{20}	180.4 km s ⁻¹
W_{50}	180.6 km s ⁻¹

Notes: The adopted center of mass is derived from the total H I distribution (Sec. 4). The H I -radius, $R_{\text{H I}}$, is the radius at which the H I surface density equals $1 M_{\odot} \text{pc}^{-2}$. W_{50} and W_{20} are the corrected widths of the global profile at 50% and 20%, respectively, calculated according to Botinelli *et al.* (1990).